TU Delft

Delft University of Technology

Effects of the rotor tip gap on the aerodynamic and aeroacoustic performance of a ducted rotor in hover

Goudswaard, Reinier J.; Ragni, Daniele; Baars, Woutijn J.

DOI
10.1016/j.ast.2024.109734

Publication date
2024

Document Version
Final published version

Published in
Aerospace Science and Technology

Citation (APA)
Goudswaard, R. J., Ragni, D., & Baars, W. J. (2024). Effects of the rotor tip gap on the aerodynamic and aeroacoustic performance of a ducted rotor in hover. *Aerospace Science and Technology*, *155*, Article 109734. https://doi.org/10.1016/j.ast.2024.109734

Important note
To cite this publication, please use the final published version (if applicable).
Please check the document version above.

Copyright
Other than for strictly personal use, it is not permitted to download, forward or distribute the text or part of it, without the consent of the author(s) and/or copyright holder(s), unless the work is under an open content license such as Creative Commons.

Takedown policy
Please contact us and provide details if you believe this document breaches copyrights.
We will remove access to the work immediately and investigate your claim.

This work is downloaded from Delft University of Technology.
For technical reasons the number of authors shown on this cover page is limited to a maximum of 10.

Aerospace Science and Technology 155 (2024) 109734

Contents lists available at ScienceDirect

Aerospace Science and Technology

journal homepage: www.elsevier.com/locate/aescte

Effects of the rotor tip gap on the aerodynamic and aeroacoustic performance of a ducted rotor in hover

Reinier J. Goudswaard, Daniele Ragni, Woutijn J. Baars *

Department of Flow Physics & Technology, Faculty of Aerospace Engineering, Delft University of Technology, 2629 HS Delft, Netherlands

ARTICLE INFO

Communicated by Damiano Casalino

Keywords:
Ducted rotor
Tip gap
Hover
Aeroacoustics

ABSTRACT

Ducted rotors are configurations known to outperform their unducted reference baselines when aerodynamic performance is concerned. Aside from aerodynamic benefits in hover, a duct also affects acoustic emissions. One of the most contended design parameters of a duct-rotor assembly is the radial distance between the blade tip and the duct wall, referred to as the "tip gap". The present study explains how the aerodynamic performance of a ducted-rotor system is affected by the tip-gap distance, taking into account the performance of the rotor and those of the duct's inlet lip and diffuser sections. Separate thrust measurements of the rotor and duct establish that the latter can generate up to half of the total thrust of the assembly. Static wall-pressure measurements along the inner wall of the duct reveal a low pressure suction zone over the duct's inlet lip area. This allows the assembly to generate more thrust than the rotor alone, even though the duct's diffuser section generates a drag component (negative thrust). From the velocity fields it is further shown that the performance-deterioration with an increasing tip gap distance is associated with a contraction of the rotor slipstream in the duct diffuser.

1. Introduction

Rapidly evolving configurations of Urban Air Mobility (UAM) and Micro Air Vehicle (MAV) concepts have shown a preference for multi-rotor systems, because of their manoeuvrability in confined areas. A multi-rotor option usually comprises a relatively large number of rotors per weight-to-be-lifted, mostly due to safety reasons, with two major aerodynamic consequences. Firstly, as the rotor area decreases, the single rotor loading increases. Secondly, the Reynolds number at which the blade sections operate also decreases. The reason for this is that a decrease in rotor area leads to a reduction of the blade's radius and the chord length. Therefore, even with an increase of the rotational frequency to ensure the same thrust, the blade-section Reynolds numbers decrease towards the laminar regime [1]. Increasing the rotor loading in a regime that is very sensitive to laminar separation leads to rotor inefficiencies, such as abrupt flow separation and a loss of system authority and control.

The scientific engineering community has opted for the usage of axisymmetric ducts to reduce the rotor loading, when the aerodynamic benefit of the duct exceeds the combined system's extra weight and aero-structural complexity. That is, a duct generally consists of an inlet lip and diffuser section, with the rotor plane positioned in the duct's throat. Fig. 1(a) provides a cross-sectional view of a ducted-rotor system, in which the rotor and duct system are of a representative relative size. Because the duct is axisymmetric, it comprises a significant volume and thus a weight penalty. For all the above reasons, ducted rotors are mostly found for propulsion systems with a relatively small diameter [2], for systems of which the thrust-to-weight ratio is larger than two, and for systems almost exclusively designed for operation in hover [3]. In multiple studies [4,5], a two-way interaction is described between the duct and the rotor, dictated by the tip-gap distance (δ_{tip}), defined as the distance between the blade tip and the wall of the duct. Therefore, the tip gap is a major parameter in the design of a ducted-rotor system. Several studies have already investigated how the tip gap affects several aspects of the aerodynamic performance of a ducted rotor [4,5,2,6–8]; these are reviewed in more depth below.

1.1. Aerodynamic and acoustic performance of ducted rotors

Compared to a single open rotor, the presence of a duct causes an increase in axial velocity at the rotor plane (velocity component W_a in Fig. 1b). If the rotational frequency of the rotor is kept the same, the tangential velocity component is unaltered ($W_t = \Omega \cdot r_A$ for rotor blade section A–A in Fig. 1b), and so for a fixed blade pitch β, the resulting effect is a net reduction of the blade loading. Concurrent with a rotor blade-loading reduction, the increased inflow angle also causes the lift

* Corresponding author.
E-mail addresses: reiniergoudswaard@hotmail.com (R.J. Goudswaard), d.ragni@tudelft.nl (D. Ragni), w.j.baars@tudelft.nl (W.J. Baars).

https://doi.org/10.1016/j.ast.2024.109734
Received 10 July 2024; Received in revised form 28 October 2024; Accepted 11 November 2024

1270-9638/© 2024 The Author(s). Published by Elsevier Masson SAS. This is an open access article under the CC BY license (http://creativecommons.org/licenses/by/4.0/).

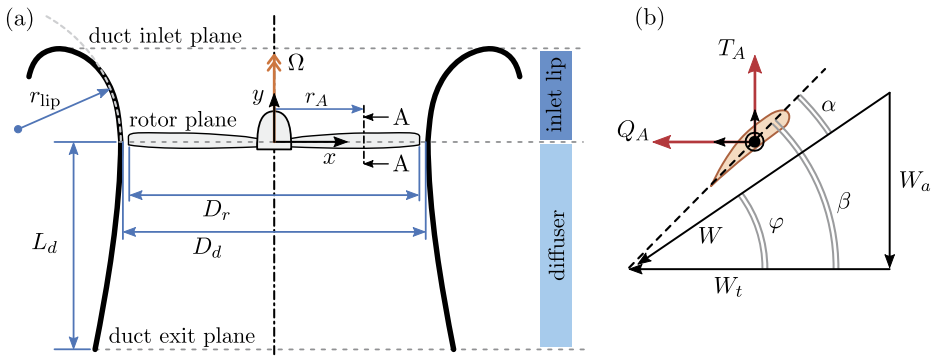

Fig. 1. (a) Schematic of a ducted-rotor system with an indication of the primary design parameters. (b) Cross-sectional view A–A of the rotor blade (section) and a velocity triangle with W_a being the axial velocity, and $W_t = \Omega \cdot r_A$ being the tangential velocity.

force to align with the torque direction, typically reducing the thrust-to-torque ratio of the rotor alone. Note that the extra power required per unit thrust is an effect only of duct installations on existing rotors (*e.g.*, [5]). Ducted-rotor systems are usually more efficient than open-rotor counterparts [4], as long as the duct is able to generate more thrust than its own weight. Pereira [5] and Martin & Tung [4] showed that for their rotor-duct assembly, the duct generated around 40% of the total thrust. Pereira [5] observed that low pressure zones over the inner and outer halves of the inlet lip of the duct are responsible for respectively 80% and 20% of the duct thrust. Even though the low pressure at the inlet lip of the duct accounts for all the extra thrust generated, the diffuser is also of great importance. In particular, for relatively long diffusers and lightly loaded rotors, an increase in the cross-sectional area along the rotor axis can enhance the slipstream deceleration, recovering part of the kinetic energy lost in the wake. Another benefit of the duct has been reported in several studies with a relatively small tip gap [6,7]. In particular, the duct wall seems to alter the formation of the blade-tip vortices and, therefore, the loss of efficiency associated with the shed circulation of the finite rotor-wing. Pereira [5] observed that this performance increase is directly transmitted to extra suction at the duct inlet-lip, which results in the duct generating (even) more thrust.

Independently of the original loading distribution of the rotor and of the duct's inlet and diffuser sections—which can be optimized by conventional techniques—the present study focuses on the change in the tip-vortex vorticity at the rotor blade tips when varying the tip gap distance. In fact, inconsistencies exist within the literature describing the flow interference of the rotor tip with the duct wall. A few details are documented, such as that a reduction of the tip gap changes the vorticity distribution of the blade-tip vortex, generally but not always resulting in extra suction at the duct inlet-lip. More in detail, an experimental study of Shukla & Komerath [7] seems to show that the presence of the duct does not change the vortical strength of the blade tip vortices, but it promotes a faster dissipation of concentrated vorticity in the helix, compared to a single rotor. In a computational study by Avallone et al. [8] on ducted wind turbines instead, a similar phenomenon brings to a full breakdown of the blade-tip vortices for small tip gaps. A different computational study by Akturk & Camci [2] indicates instead that the reason for the enhanced suction over the duct's inlet section is the blockage of the tip leakage flow. Studies by Bento et al. [6] and Martin & Tung [4] attribute a zone of flow reversal along the wall of the duct, just behind the rotor plane, to the critical interaction of the rotor tip vortex with the duct's boundary layer. In summary, predicting the actual performance of a duct-rotor assembly requires a combined understanding of the complex mutual interactions between the rotor flow and the duct geometry.

When focusing on the acoustic emissions of ducted-rotor systems, the number of studies is limited, with only a few reporting changes in the far-field noise magnitudes [9,7,8,10]. A consensus amongst these studies is that the noise intensity of the duct-rotor assembly increases when the rotor is closer to the duct wall. Whether this is caused by the onset of a secondary noise source at the tip gap, or due to the enhancement of the unsteady flow at the rotor blade, remains unknown. In particular, this is because the change in rotor performance with an increase of axial velocity—due to the presence of the duct—causes a change in the loading and thickness noise. In the work of Avallone et al. [8], an increased broadband noise intensity was observed in the smaller tip gap cases. They ascribed this effect to an equivalent additional noise source, caused by an enhancement of flow separation (velocity fluctuations) along the duct diffuser wall, created by the sweeping blade. A simultaneous assessment of the change in aerodynamic performance is critical to accurately determine the change in noise sources and emissions.

1.2. Current contributions and outline

Our current study aims to explain how the tip gap affects the aeroacoustic performance of a small-scale ducted rotor in hover. Leaving aside the optimization of a specific duct design, this study elucidates the link between the aerodynamic performance of a reference duct design and the rotor flow created at the tip gap. Particular attention will be on the interaction between the rotor-induced flow and the adverse pressure gradient flow along the diverging diffuser wall.

The manuscript is organized as follows: an experimental campaign has been conducted with a ducted rotor in hover, described in section 2. Aerodynamic analyses are presented in section 3, outlining both the integral performance of the system as well as assessments of the internal flow. Section 4 focuses on the acoustic results, before section 5 provides concluding remarks.

2. Experimental setup and methodology

2.1. Facility and ducted-rotor system

Experiments were conducted in the laboratory of the Department of Flow Physics & Technology at the Delft University of Technology. A small-scale ducted rotor-in-hover was constructed and is a reference, representative of conventional ones used on MAVs in hover. In particular, the ducted-rotor system and operating conditions are comparable to propulsive units on a Flyability Elios 3 (a 1.9 to 2.3 kg ducted quadcopter drone, see https://www.flyability.com/elios-3) that inspired the system design with the duct. Details of the duct design are included in Appendix A, while a schematic of the ducted-rotor system is shown in Fig. 1 (with photographs in Fig. 2). A T-motor F80 PRO KV1530 was used to propel the rotor. The duct diameter, defined as the diameter at the throat, equals $D_d = 128.1$ mm. The rotor diameter D_r is parametrically varied, with 6 rotors comprising diameters from $D_r = 127.2$ mm down to $D_r = 124.9$ mm. This results in tip-gap ratios (tip gap distance as the percentage of duct throat diameter D_d) ranging between $\delta^*_{\text{tip}} = 0.625\%$ and 2.422%.

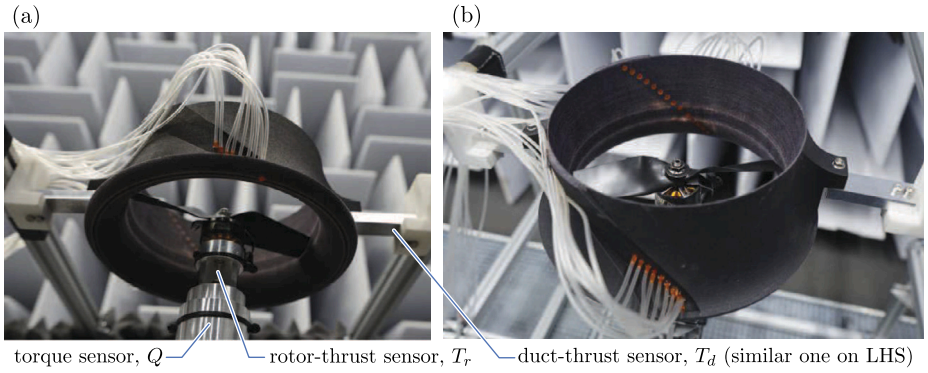

Fig. 2. (a,b) Photographs of the small-scale ducted-rotor system (note that the setup is inverted with the thrust force pointing down). Load cells are annotated and include one torque sensor, one rotor-thrust sensor, and two duct-thrust sensors (one on either side of the duct). Static wall-pressure ports are also visible along the duct inlet and diffuser sections (pressure tubing was removed during force measurements).

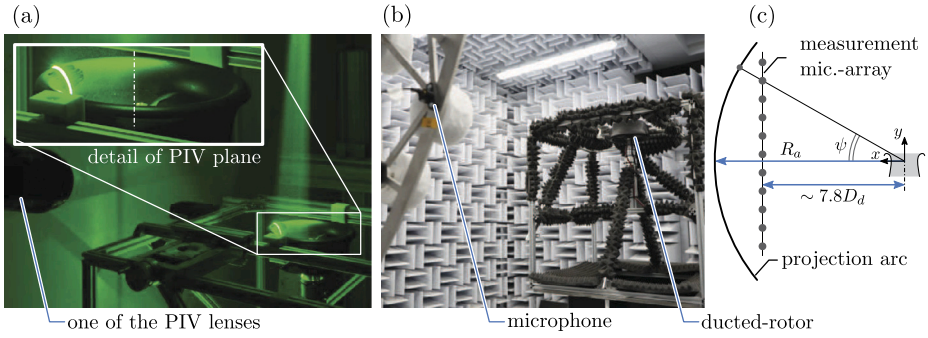

Fig. 3. Photographs of (a) the stereoscopic PIV setup for acquiring the internal flow field through the duct, and (b) microphones for capturing the far-field acoustic signature. (c) Schematic of the microphone measurement-array and a virtual arc of radius $R_a = 10D_d$ to which the acoustic data are projected.

2.2. Flow measurements with PIV

A stereoscopic particle image velocimetry (PIV) setup is employed to image the velocity field in the (x, y) mid-plane of the duct (see Fig. 3a); this yields mean velocity fields, trajectories of blade tip vortices, their strength, and possibly their breakdown. The aim is to visualize the flow structures generated by the rotor, and their interaction with the duct wall. Two LaVision sCMOS 16 bit, 4 Mpx resolution cameras were used, comprising a pixel size of 6.5 μm. Both cameras were equipped with 105 μm Nikon Micro-Nikkor lenses to image a field-of-view of approximately 4 cm × 2 cm. Safex smoke seeding particles with a median diameter of 1 μm were illuminated by a Quantel EverGreen200 Double-Pulse Nd:YAG laser (532 nm wavelength, 200 mJ per pulse). Laser optics conveyed the illumination, forming a laser sheet of about 1.5 mm thickness. Synchronization of the laser pulses and image acquisition was ensured by a LaVision programmable timing unit in combination with the LaVision DaVis 10.1 software package. Sets of 500 images were acquired at 15 Hz and these comprised instants of the velocity field that were random with respect to the rotor's azimuthal position (these were used for computing mean velocity fields above and below the rotor plane). In addition, sets of 500 images were acquired in a phase-locked sense, by synchronizing the PIV acquisition to several rotor positions using a 1-per-revolution trigger signal. Phase-locked fields of the mean velocity were used to examine the helix of concentrated vorticity originating from the rotor blade-tips. A multi-pass cross-correlation procedure was adopted with a final interrogation window of 16 px × 16 px and 75% overlap. This window results in a final average concentration of 4 particles per window, which constitutes an appropriate seeding concentration [11]. Calibration of the field-of-view and self-calibration, for aligning the imaged volume with the illuminated one, was conducted using a LaVision Type-7 calibration plate. Convergence of the mean and statistics was verified within the batch of the 500 processed vector fields.

2.3. Pressure and force measurements

For measuring the integral performance of the duct and rotor, several load cells were used (Fig. 2). The duct was equipped and supported with two identical load cells on either side, to measure its thrust, T_d. These load cells were ME-Meßsysteme, model KD45 5N,[1] double bending beam force sensors with a maximum nominal force of 5 N. Simultaneously, the rotor-motor assembly was mounted to a load cell to measure the rotor thrust, T_r, and rotor torque, Q. For the thrust force a FUTEK, model LSB200,[2] miniature S-beam loadcell was used with a maximum load capacity of ~22 N (5 lb). Finally, for the torque a Transducer Techniques, model RTS-25[3] reaction torque sensor was used with a capacity range of ~1.8 Nm (25 oz-in). All load cells had an accuracy of ±0.1% full-scale output. Force measurements were acquired for 10 seconds at each constant rpm value, at a sampling frequency of 25.6 kHz, and only mean values are considered in this work. The static pressure profile along the duct's inner wall is measured at 24 different axial locations. At each location, 3D-printed inserts were mounted to achieve pressure taps of 0.2 mm in diameter. The inner surface of the duct is sanded smooth with these inserts. The static wall-pressure was measured with differential pressure transducers, with the atmospheric pressure as reference. A series of Honeywell TruStability® High Accuracy Silicon Ceramic (HSC) piezoresistive silicon pressure sensor were used, with a 2500 Pa full-scale span (FSS) and an accuracy of ±0.25% FSS. Each measurement of the static wall-pressure was acquired for a duration of 30 seconds at each constant rpm value, at a sampling frequency of 200 Hz.

[1] https://www.me-systeme.de/en/kd45-5n.
[2] https://www.futek.com/store/load-cells/s-beam-load-cells/miniature-s-beam-LSB200/QSH02069.
[3] https://www.transducertechniques.com/rts-torque-sensor.aspx.

2.4. Acoustic measurements

Acoustic measurements were conducted in an anechoic facility at the Delft University of Technology [12]. A linear array of 11 microphones was positioned vertically (in parallel with the rotor-axis). The array was positioned at a distance of $\sim 7.8 D_d$ from the rotor hub, see Fig. 3(c). For each operating condition, the acoustic measurements with the microphone array were repeated at two different positions. That is, the microphone array was once traversed vertically to obtain a larger range of microphone angles; data were merged in post-processing and governed a relatively large angular range of the far-field directivity angle, ψ (spanning $-49° \lesssim \psi \lesssim 52°$).

As sensors, GRAS 40PH-10 1/4" CCP free-field microphones were used with a frequency range between 10 Hz and 20 kHz. Data were acquired for two different tip gaps of the ducted-rotor system, and at two rotor rpm-values of 11000 rpm and 12000 rpm. For each operating condition, all microphone signals were recorded for 30 seconds, at a sampling frequency of 51.2 kHz.

In post-processing, acoustic spectra were first calculated from each acoustic time series, $p(t)$. For this, the one-sided spectrum $\phi_{pp}(f) = 2\langle P(f)P^*(f)\rangle$ was computed, where $P(f) = \mathcal{F}[p(t)]$ is the temporal FFT and $\langle\cdot\rangle$ denotes ensemble-averaging. A sound pressure spectrum level (SPSL) in dB follows from $\mathrm{SPSL}(f) = 10\log_{10}(\phi_{pp}(f)/p_{\mathrm{ref}}^2)$, with $p_{\mathrm{ref}} = 20\,\mu\mathrm{Pa}/\sqrt{\mathrm{Hz}}$. Ensemble-averaging was conducted using FFT partitions of $N = 16 f_s/\omega$ samples, to ensure that the discrete frequencies align with the blade passing frequency (BPF) and its harmonics; this reduces the leakage of tonal energies into neighboring frequencies [13]. The value of N yields a spectral resolution of $\mathrm{d}f = 12.5$ Hz and 750 ensembles with 50% overlap. For all analyses, the raw pressure time series were subject to a band-pass filter, with a flat response between 60 Hz and 15 kHz, suppressing the non-anechoic, low-frequency content [12] and the energy beyond the highest frequency range of the microphone. Acoustic data were also projected[4] to a circular arc with a constant radius of $R_a = 10 D_d$ (recall Fig. 3c). For the far-field directivity patterns, the overall sound pressure level (OASPL) was computed by integrating the final acoustic spectra.

2.5. Operating conditions and performance coefficients

To evaluate performance coefficients, all load measurements are carried out over a sequence of rotational speeds ranging from 2000 rpm to 14000 rpm, with increments of 1000 rpm. PIV and acoustic measurements were only performed at 11000 rpm and 12000 rpm; these correspond to a total thrust of respectively 4.7 N and 5.8 N for the two rpm-values corresponding to the configuration with the smallest tip gap. For quantifying the aerodynamic performance of the ducted rotor, the duct thrust, T_d, is considered, as well as the rotor thrust, T_r, and rotor torque, Q. Using these quantities, the power coefficient C_P, rotor and/or duct thrust coefficient C_T, and the system's figure of merit, FM, can be formulated as follows:

$$C_P = \frac{P}{\rho A v_{\mathrm{tip}}^3}, \quad C_T = \frac{T}{\rho A v_{\mathrm{tip}}^2}, \quad FM = \frac{C_T^{1.5}}{\sqrt{2} C_P}. \tag{1}$$

Here ρ is the air density, and area $A = \pi D_d^2/4$ is computed with the duct diameter (instead of with the rotor diameter D_r that is varying with each different tip-gap ratio). The rotor tip speed v_{tip} and mechanical power P are a function of the rotational speed of the rotor, Ω (in terms of rpm), the rotor diameter, D_r, and the rotor torque, Q:

$$v_{\mathrm{tip}} = \Omega \cdot \frac{2\pi}{60} \cdot \frac{D_r}{2}, \quad P = \Omega \cdot \frac{2\pi}{60} \cdot Q. \tag{2}$$

[4] Projections of the acoustic data included corrections for the inverse-square law of the acoustic intensity, as well as the frequency-dependent corrections for atmospheric absorption (details in [14]).

The above-defined coefficients capture the integral performance of the ducted-rotor system. To further inspect the origin of the loading, the static pressure distribution over the duct's inner wall is considered. It is used to determine which areas of the duct effectively contribute to the duct thrust T_d, and how this changes for different tip gaps. The static pressure coefficient normalized with the dynamic pressure at the blade-tip is a function of the static pressure, p, and the atmospheric pressure in the environment, p_∞:

$$C_{p,\mathrm{stat}} = \frac{p - p_\infty}{\frac{1}{2}\rho v_{\mathrm{tip}}^2}. \tag{3}$$

In the results section, the non-dimensional performance coefficients, C_T, C_P and FM, as well as profiles of the pressure coefficient $C_{p,\mathrm{stat}}$, are presented for a rotational speed of $\Omega = 11000$ rpm. Based on the transducer accuracy's listed in section 2.3, the uncertainty in these coefficients is less than $C_T \pm 2.7 \cdot 10^{-4}$, $C_P \pm 3.4 \cdot 10^{-4}$, $FM \pm 3.9 \cdot 10^{-2}$, and $C_{p,\mathrm{stat}} \pm 1.9 \cdot 10^{-3}$. These uncertainties are indicated with error bars in Fig. 6 and Fig. 7(b); observations made throughout our work are based on data trends exceeding the measurement uncertainty.

3. Tip gap effect on the aerodynamic performance

3.1. Aerodynamic performance

To evaluate the aerodynamic performance of the system, the duct thrust (T_d) and rotor thrust (T_r) are first plotted for the smallest tip-gap ratio in Fig. 4(a). The total thrust is simply taken as the sum, $T_{\mathrm{tot}} = T_d + T_r$. Alongside, in Fig. 4(b), the rotor torque (Q) is plotted. In the present configuration, the duct generates more thrust than the rotor, contributing ~55% to the total thrust at an operating condition of $\Omega = 11000$ rpm. This result highlights the immense contribution of the duct-thrust to the total thrust. This is later focused on when non-dimensional performance parameters are examined.

We now concentrate on one rpm-operating value only (around 11000 rpm, near the highest value studied). In Fig. 5, the rotor thrust is shown as a function of the tip-gap ratio corresponding to the six separate rotors. It is evident that while the rotor thrust T_r is unaffected by the vicinity of the blade tip (vortex) to the duct wall, the duct thrust T_d strongly decreases with an increase in the tip-gap ratio. In line with the studies of Pereira [5] and Martin [4], a ~37% thrust reduction (from 2.7 N to 1.7 N) is measured when the tip-gap ratio increases from 0.625% to 2.422%. Provided that the rotor thrust does not vary with the tip gap, the slipstream-induced velocity and the rotor-induced helix of concentrated vorticity should remain unaltered with different tip-gap distances. Therefore, the reduction in duct thrust must be determined by the slipstream development along the duct wall.

Non-dimensional performance coefficients are considered next in Fig. 6, and plotted as a function of the tip-gap ratio, δ_{tip}^*. As expected, minor variations of thrust and torque coefficients are seen for the rotor. Conversely, an overall efficiency decrease of the system becomes evident from a decreasing figure of merit, FM, and is caused by a lower duct thrust for an increase in tip-gap ratio. It has to be noted that the figure of merit of the entire system is not bounded by one, since the reference diameter of the duct throat is used in the actuator disk area (recall section 2.5). Arguably, a correct normalization would entail a larger actuator disc area, which should represent the overall effect of the duct inlet lip (also effectively contributing to the total thrust). Nevertheless, choosing such a representative area is non-trivial and hence the current duct throat area of $A = \pi D_d^2/4$ is kept for comparison with the existing literature [4,5].

3.2. Flow field and pressure distribution within the duct

An acceleration and deceleration of the flow throughout the duct affect the imprint of the wall-pressure distribution and, thus, the resulting force on the (internal) duct. Fig. 7(a) visualizes the pressure distribution

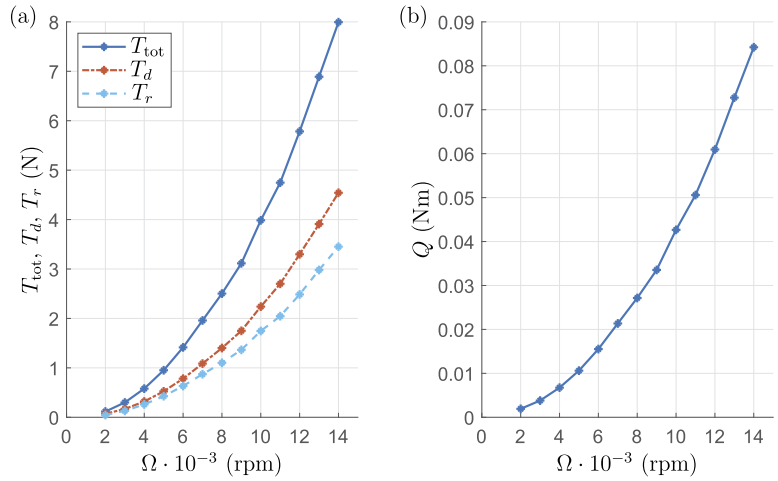

Fig. 4. Load-cell performance measurements on the ducted-rotor system: (a) Thrust generated by the duct T_d, rotor T_r, and their sum T_{tot}, and (b) torque on the rotor. Both as a function of the rotational speed Ω, and with a tip gap of $\delta^*_{tip} = 0.625\%$.

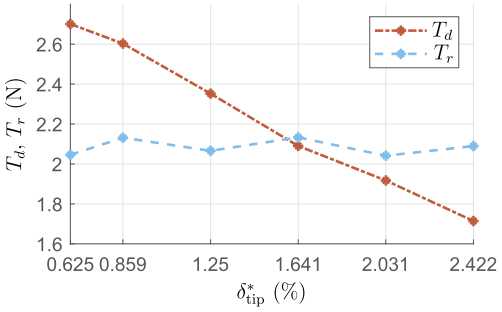

Fig. 5. Thrust of the duct T_d and of the rotor T_r, as a function of the tip-gap ratio δ^*_{tip}, at a rotational speed of $\Omega = 11000$ rpm.

by way of showing pressure profiles directly over the cross-section of the duct contour. Two profiles are shown, corresponding to the largest and the smallest tip-gap ratio at $\Omega = 11000$ rpm.[5] A larger distance of the pressure profile, away from the duct-contour, corresponds to a larger negative relative pressure (larger suction), with respect to the ambient one. Alongside, in Fig. 7(b), profiles of the pressure coefficient $C_{p,stat}$ are plotted against the duct length coordinate, L. Clearly, the contribution of the static pressure is lower than the ambient pressure along the entire duct's surface, except for the stagnation point at the most outward position of the duct lip. The strongest suction is localized over the inlet lip, after which the largest pressure gradient (increase in pressure) occurs at the rotor plane. This pressure increase consists of large initial jump, followed by a small secondary suction zone near $y/D_d \approx -0.1$ (labeled in Fig. 7b). The strength of suction in this secondary suction zone is on the order of the measurement uncertainty, but was consistently observed in repeating measurements. This small suction peak is therefore presumably linked to the signature of a rotor tip vortex close to the duct wall, as has been observed by others [5,16]. Downstream of it, the static pressure increases rapidly again, after which it continues to rise inside the duct's diffuser up to the exit plane at $y/D_d = -0.35$ where the pressure equalizes to the ambient pressure. Therefore, despite the axial pressure difference imposed by the rotor at a specific thrust setting, the duct lip and diffuser designs guarantee the favorable and adverse pressure gradients, respectively. These pressure gradients effectively build up the duct's thrust contribution.

[5] Results of pressure distributions for more tip gaps and operating conditions can be found in a thesis by Goudswaard [15], archived in the TU Delft repository: http://resolver.tudelft.nl/uuid:727fd73b-ddb1-40d9-b7fd-2617f769136d.

Table 1
Individual contributions of the inlet lip and diffuser to the total duct thrust, T_d. Forces are obtained by integrating the static-pressure results over the duct profile; load-cell results are included for comparison. Results are shown for the two different tip-gap ratios δ^*_{tip} considered in Fig. 7 and for the same rotational speed of $\Omega = 11000$ rpm.

	T_d (N) (Static-pressure)			T_d (N) (Load-cell)
	Inlet lip	**Diffuser**	**Total**	**Total**
$\delta^*_{tip} = 0.625\%$	2.9381	-0.0724	2.8657	2.7109
$\delta^*_{tip} = 2.422\%$	1.7801	-0.0389	1.7412	1.7143

It has to be noted that the inlet lip ($L > 0$) is the only location where the vectorial contributions of the surface area-elements have a component pointing in the thrust direction (positive y direction). As can be seen from Fig. 7, the diffuser ($L < 0$) elements yield contributions in the opposite direction (*i.e.*, downwards). Thus, suction in the duct diffuser results in a negative contribution to the total duct thrust. Despite that, the diffuser allows for a full recovery of the pressure downstream of the rotor plane, promoting a large and beneficial flow acceleration at the inlet lip. To quantify the net thrust of the duct, Table 1 lists the two thrust contributions of the inlet and diffuser sections of the duct, for the different tip-gap ratios. Values provided are in Newton and were inferred by integrating the vertical contributions of the static wall-pressure profiles along the duct's inner wall. Even though the static wall-pressure measurements were spatially sparse, the integration errors are minor given that net thrust of the duct, inferred via the pressure integration, agrees exceptionally well with the integral value measured using the load cells (*e.g.*, for the $\delta^*_{tip} = 2.422\%$ case 1.7412 N versus 1.7143 N, yielding an error of less than 2%). The pressure profiles along the duct wall that a design guideline for the rotor's axial location is such that the pressure-increase, created by the rotor operating at a specific thrust setting, is such that it compensates for the full pressure recovery within the diffuser. Only then the inlet lip and diffuser will operate as a cambered airfoil without any extra pressure contribution in the downward direction.

In addition to the load-cell and static-pressure measurements, PIV measurements provide insight into the flow topology within the duct. Fig. 8 presents the mean velocity magnitude for two tip-gap ratios. While the maximum induced velocity in the slipstream is almost identical, the flow velocity-magnitude at the inlet lip is higher for the smaller tip gap. This higher flow velocity persists downstream of the rotor plane, and in the region close to the diffuser wall. Our quantitative flow visualizations strengthen the earlier observations in that the small tip gap promotes

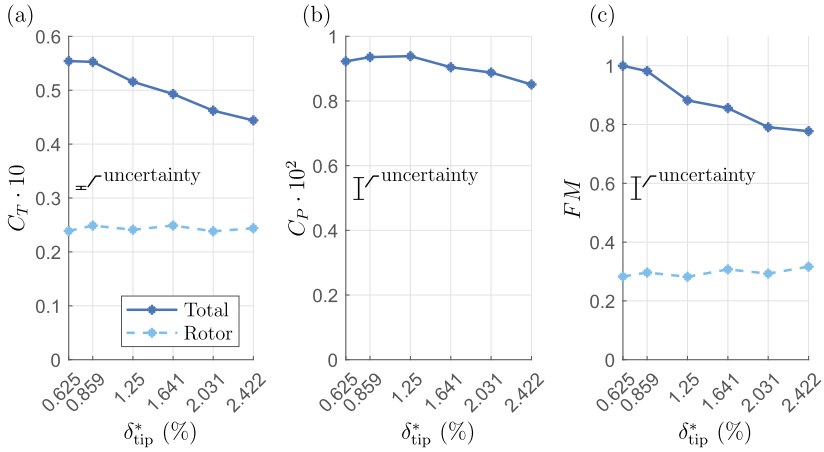

Fig. 6. Performance coefficients of the ducted-rotor system as a function of the tip-gap ratio δ^*_{tip}, at a rotational speed of $\Omega = 11000$ rpm: (a) Thrust coefficient, C_T, (b) power coefficient, C_P, (c) figure of merit, FM. Maximum uncertainties in these coefficients are represented with the error bars, and are described in section 2.5.

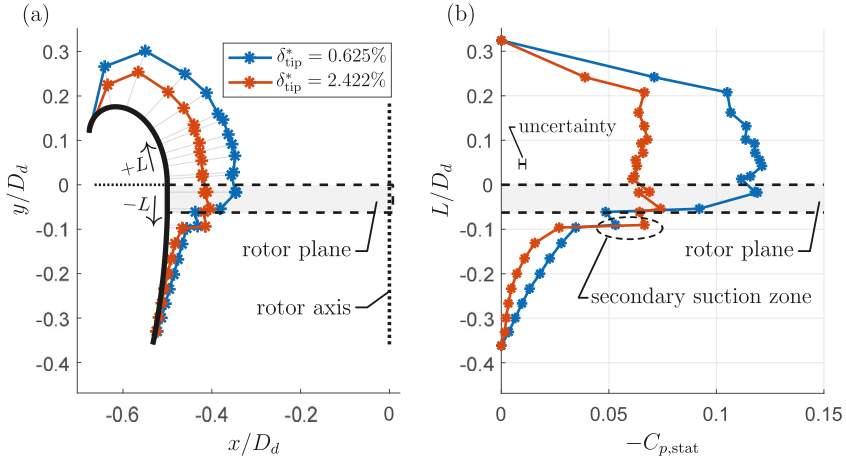

Fig. 7. Static-pressure measurements on the duct's inner wall: (a) Visualization of the negative pressure distribution over the duct contour, (b) static pressure coefficient, $C_{p,\text{stat}}$, plotted against the duct length coordinate, L. Results are shown for two different tip-gap ratios δ^*_{tip} and for a rotational speed of $\Omega = 11000$ rpm. The uncertainty in $C_{p,\text{stat}}$ is represented with the error bar in sub-figure (b), and is described in section 2.5. (For interpretation of the colors in the figure(s), the reader is referred to the web version of this article.)

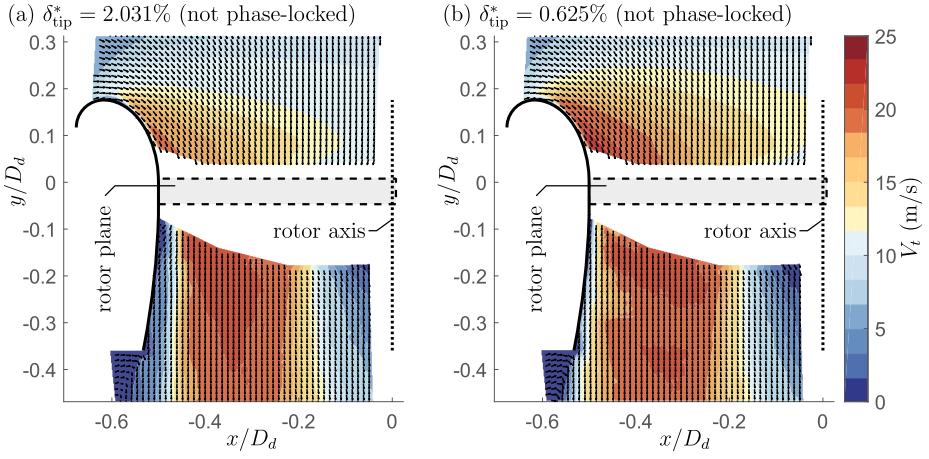

Fig. 8. Contour of total velocity V_t in the axial-radial mid-plane of the ducted-rotor system for tip-gap ratios of (a) $\delta^*_{\text{tip}} = 2.031\%$ and (b) $\delta^*_{\text{tip}} = 0.625\%$, for the same rotational speed of $\Omega = 11000$ rpm. Velocity fields are formed by averaging fields corresponding to random azimuthal positions of the rotor.

a larger flow acceleration over the duct lip and, thus, an increase in suction.

For the cases with a small and large tip-gap ratio, it was shown that the rotor performance is similar. Hence, it is unclear what phenomenon is responsible for the increased suction at the lip location when the smaller tip gap is concerned. Results of the phase-locked PIV acquisition were proven to be insightful on this matter. Velocity results are shown in Fig. 9, for one phase of $\theta = 90°$ (with a deviation of $\pm 7°$), meaning that

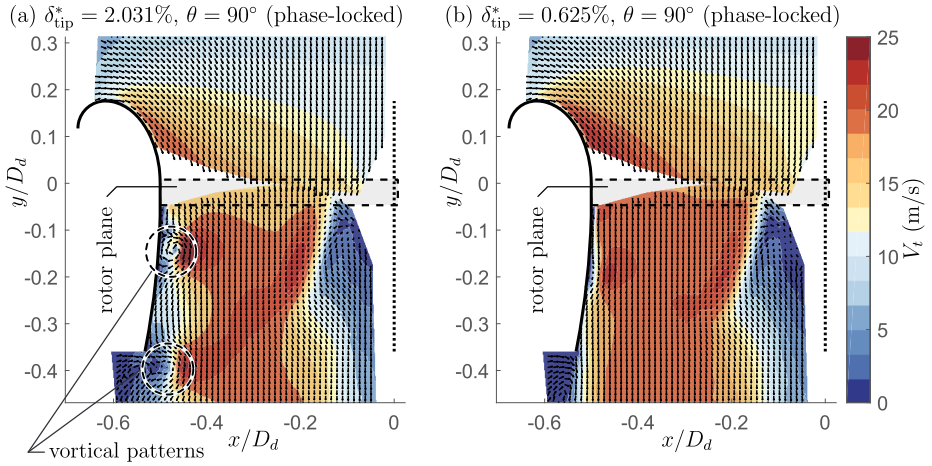

Fig. 9. Contour of total velocity V_t in the axial-radial mid-plane of the ducted-rotor system for tip-gap ratios of (a) $\delta^*_{tip} = 2.031\%$ and (b) $\delta^*_{tip} = 0.625\%$, for the same rotational speed of $\Omega = 11000$ rpm. Velocity fields are phase-locked to a $\theta = 90°$ azimuthal position of the rotor.

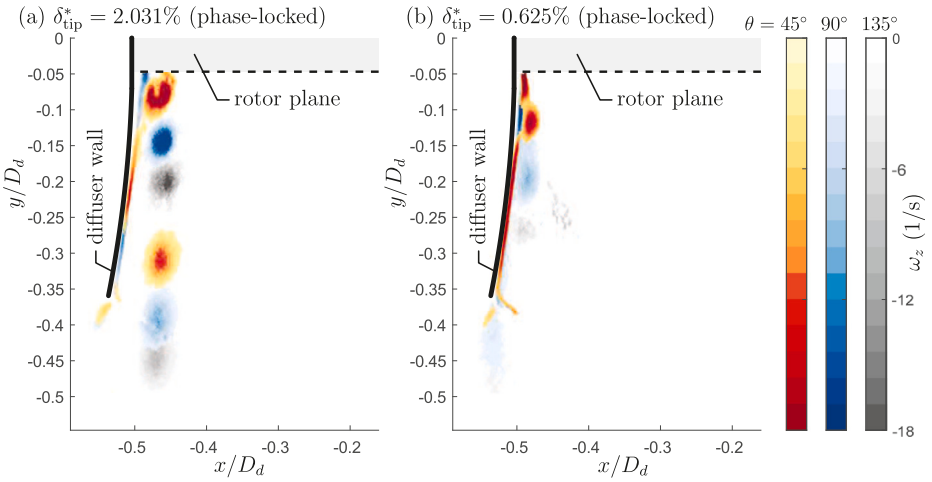

Fig. 10. Phase-locked ($\theta = 45°$, $\theta = 90°$ and $\theta = 135°$) vorticity fields in the axial-radial plane of the duct: Vorticity ω_z plotted against x- and y-coordinates for tip-gap ratio's (a) $\delta^*_{tip} = 2.031\%$ and (b) $\delta^*_{tip} = 0.625\%$, for the same rotational speed of $\Omega = 11000$ rpm.

the phase-locked velocity fields are averaged from 500 instantaneous velocity fields for which the rotor is positioned in-line with the z axis. From the phase-locked contour of velocity magnitude, superimposed to the vector field displaying the in-plane velocity, it is possible to observe the cross-sectional cut of the slipstream helix in the traces of the vortical patterns close to the duct wall for the large tip gap case (labeled regions in Fig. 9(a) at axial locations of $y/D_d \approx -0.14$ and $y/D_d \approx -0.4$). On the contrary, for the case with the smallest tip gap presented in Fig. 9(b), only residual traces of vorticity are present. Aside from the differences in vortical patterns in the near vicinity of the duct wall, a relatively large region of reduced downward velocity penetrating in-board is present in the case of the large tip gap, at an axial location in between the vortical patterns. At the same time, a wake sheet comprising a relative high downward velocity appears most pronounced in relation to the lower vortical pattern.

When explaining the performance of the diffuser (directly linked to its ability to decelerate the expanding the flow), the flow topology near the wall needs to be understood. For this, we further concentrate on the evolution of the vorticity generated by the slipstream. Fig. 10 tracks the evolution of vorticity regions, by plotting the out-of-plane vorticity ω_z from the stereoscopic flow field for three different azimuthal positions of the rotor (phases of $\theta = 45°$, $\theta = 90°$ and $\theta = 135°$). For the large tip gap, the interaction between the rotor-induced flow and the flow along the duct wall is such that the diffuser's effect opposes the slipstream contraction, resulting in slipstream trajectory not adhering to the diffuser-contour. The rotating vortex flow displaces streamwise momentum in the radial direction and prohibits the formation of a uniform induction field downstream of the rotor (see also Fig. 8). The small tip gap inhibits the formation of a coherent tip vortex, but produces a stretched and more diffused vortical field that does not substantially decelerate the mean flow along the diffuser wall, and is able to expand and adhere to the duct's wall. The pressure-recovery that is now present indirectly generates the superior flow acceleration above the rotor plane: the mean total velocity reaches higher values along the duct lip in case of the small tip-gap ratio (Fig. 8b cf. Fig. 8a), and in addition the more uniform flow deceleration within the diffuser also results in a larger rotor-inflow velocity along the entire rotor span.

Summarizing our findings based on the aerodynamic data, we can conclude that:

- reducing the tip gap to a minimum creates a blockage of the tip-leakage flow, generated by the blade loading across the rotor (jump in pressure across the rotor plane). The vorticity might be localized or diffused depending on the ratio between the tip gap and the tip vortex size;
- a coherent vortical distribution of velocity in the blade-tip vortex helix promotes the transfer of streamwise momentum away from the diffuser's wall. Consequently, the region of lower axial velocity

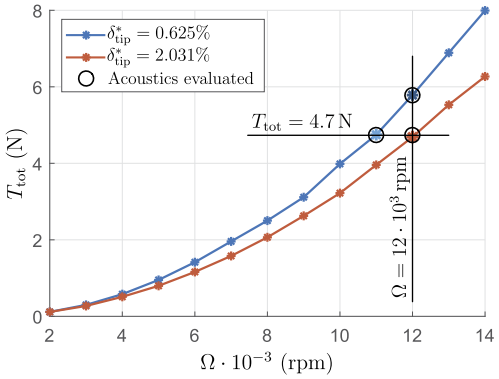

Fig. 11. Illustration of the three operating conditions for the acoustic measurements (open circles), covering a constant total thrust setting T_{tot}, and a constant rotational speed setting Ω, for the two different tip-gap ratios δ^*_{tip}.

near the wall reduces the pressure-recovery effect, and thereby the maximum possible suction at the duct inlet lip;

- tip vortex trajectories are indicative of the rotor's slipstream development and can be informative about whether a diffuser works adequately. That is, when the helix of concentrated vorticity is *not* adhering to the diffuser wall, due to an aggressive area expansion, the slipstream below the rotor contracts and renders the diffuser ineffective in generating a low pressure zone at the duct's inlet section;
- over-constraining the lip curvature has no effect unless the diffuser is able to process the imposed pressure jump associated with the thrust-generating rotor.

From a design point-of-view, the previous observations suggest that an optimal duct performance is achieved through the following steps. Firstly, the jump in pressure across the rotor plane, as well as the tip-vortex size, should be determined for a specific blade loading. The tip-gap should be sized smaller than the size of the tip vortex. Given a specific profile for the lip and diffuser (*i.e.*, one similar to the outline of the suction-side of a conventional airfoil), the axial position of the rotor should be such that the jump in pressure of the rotor remains lower than the pressure recovery of the flow from a position just downstream of the rotor, to one at the exit plane of the duct.

4. Tip gap effect on the acoustic performance

In addition to the aerodynamic performance study, acoustic measurements were conducted to investigate the effect of the tip-gap ratio on the far-field acoustics of the ducted-rotor system. Comparisons of the acoustic results for different tip-gap ratios can be made at settings of constant total thrust, or constant rotational speed. Here we consider both by evaluating three operating conditions, illustrated in Fig. 11, comprising a constant thrust setting of $T_{tot} = 4.7$ N, and a constant rotational speed setting of $\Omega = 12000$ rpm, for the two tip-gap ratios of $\delta^*_{tip} = 0.625\%$ and $\delta^*_{tip} = 2.031\%$.

First, the overall sound pressure level (OASPL) for all microphone positions in the array is considered by way of the noise directivity pattern presented in Fig. 12. Generally, for all three operating conditions, the noise directivity follows a bi-lobed pattern that is common for rotors operating at high loading conditions [14]. That is, the pattern is dominated by the thickness and loading contributions peaking at roughly $+/-$ 30 degrees from the rotor plane [17]. Before describing how the tip-gap ratio affects the far-field acoustics, we introduce acoustic spectra as the frequency-dependence is critical in evaluating the change in acoustic intensity. Acoustic spectra are presented in Fig. 13 and consider acoustic data at three different directivity angles: $\psi = 38.5°$ (region upstream of the rotor, Fig. 13a), $\psi = -7.7°$ (sideline region, Fig. 13b) and $\psi = -39.9°$ (downstream region, Fig. 13c); the exact angles are indicated in Fig. 12. For each directivity angle, three acoustic spectra are presented and correspond to the three operating conditions that were illustrated in Fig. 11.

When comparing the OASPL for the two different tip-gap ratios, at the same rotational speed ($\Omega = 12000$ rpm), the small tip gap increases the acoustic pressure intensity. Our PIV experiments revealed that the velocity at the duct outlet, near the diffuser's trailing edge, increases for the smaller tip-gap ratio. This higher velocity should enhance the high-frequency component of the noise and this is reflected in the high-frequency portions of the spectra, at all three directivity angles (*e.g.*, the orange spectra are noticeably lower for roughly $f/f_b > 10$). At the same time, the tonal noise (particularly the spectral peak at the BPF) is of a similar magnitude because of the same rotational speed. Hence, a smaller tip-gap ratio, at the same rotational speed, increases the OASPL solely due to the increase of high-frequency noise at all directivity angles.

In practical scenarios, a propulsive unit, on for instance a drone, should deliver a certain amount of prescribed thrust. And so, it is desirable to examine the change in the far-field acoustic pressure intensity for the two different tip-gap ratios, at the same produced total thrust ($T_{tot} = 4.7$ N). From Fig. 12 it becomes apparent that a smaller tip-gap ratio decreases the OASPL over the full directivity range. A primary cause for this reduction is the smaller contribution to the acoustic imprint of the rotor loading and thickness noise, because the duct is producing a significantly larger fraction of the total thrust. This decrease in rotor loading and thickness noise is evident from the lower spectral peak at the BPF and higher harmonics in Figs. 13(a-c). So even though the high-frequency noise is enhanced due to the higher diffuser-exit velocity, the reduction in tonal noise dominates.

5. Conclusions

An experimental study was conducted to elucidate the mutual interaction between a reference rotor and a reference duct in a ducted-rotor system in hover conditions. The study focused on the aerodynamic propulsive performance with respect to the tip-gap distance. Static pressure distributions on the duct's inner wall revealed the thrust-generation effectiveness of the inlet lip in combination with a duct diffuser. In addition, axial-radial planes of PIV-based velocity throughout the entire duct fostered the vortical flow features induced by the rotor blades, and their effect on the adverse-pressure gradient flow near the duct's diffuser wall. Finally, far-field acoustic pressure signals were acquired to accentuate the differences in emitted noise with varying operation regimes.

Our current study confirms that the duct generates a large proportion of the total thrust of the ducted-rotor system, which is localized mostly at the inlet lip. Despite negatively contributing to the thrust, the diffuser determines the pressure recovery below the rotor, enhancing the latter's performance and overcoming its own losses. The highest performance achieved is obtained for a tip gap of 0.625% corresponding to an extra thrust of 40% solely generated by the duct, resulting in a 20% higher-figure of merit of the system. The rotor thrust for this specific study is insensitive to the tip-gap, mainly due to the relatively low design angle of attack at the tip. The performance increase with a smaller tip gap is related to the breakdown of rotor tip vortices and an increased axial velocity in the duct. The PIV measurements confirm that a small gap reduces the tip flow leakage and the formation of tip vorticity. As the tip gap increases, the combination of the diffuser deceleration with the convecting tip vorticity from the slipstream determines the formation of a region of low axial velocity near the duct's diffuser wall, promoting the reduction of the extra thrust of the duct. When comparing the noise emission at constant thrust, the microphone measurements obviously show that a smaller tip gap decreases the overall noise due to the reduced contribution of the rotor loading and thickness and the increased contribution in loading of the duct. When comparing at the same rpm value, a smaller tip-gap ratio increases the overall noise as the exit

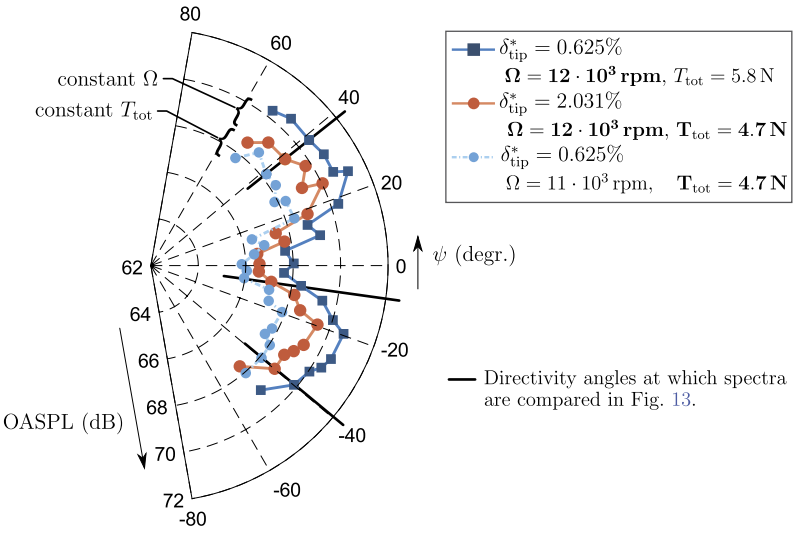

Fig. 12. Overall sound pressure level (OASPL) at a distance of $R_a = 10D_d$, plotted against the directivity angle, ψ. Directivity patterns are compare two tip-gap ratios δ^*_{tip}, at the same rotational speed ($\Omega = 12000$ rpm), as well as at the same level of thrust ($T_{tot} = 4.7$ N). Recall that the three corresponding operating conditions were illustrated in Fig. 11.

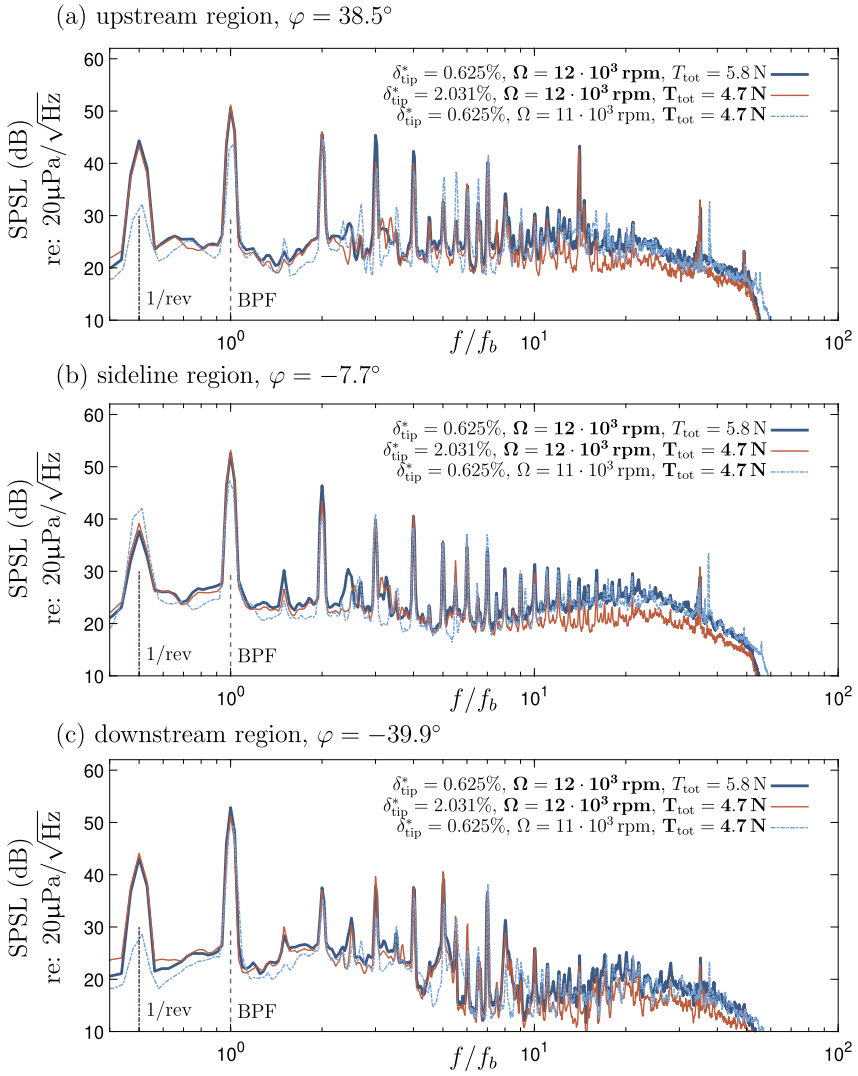

Fig. 13. Acoustic spectra in the (a) upstream, (b) sideline, and (c) downstream regions of the acoustic field; directivity angles are indicated above each set of spectra. Each set of spectra compares two tip-gap ratios δ^*_{tip}, at the same rotational speed ($\Omega = 12000$ rpm), as well as at the same level of total thrust ($T_{tot} = 4.7$ N). Recall that the three corresponding operating conditions were illustrated in Fig. 11.

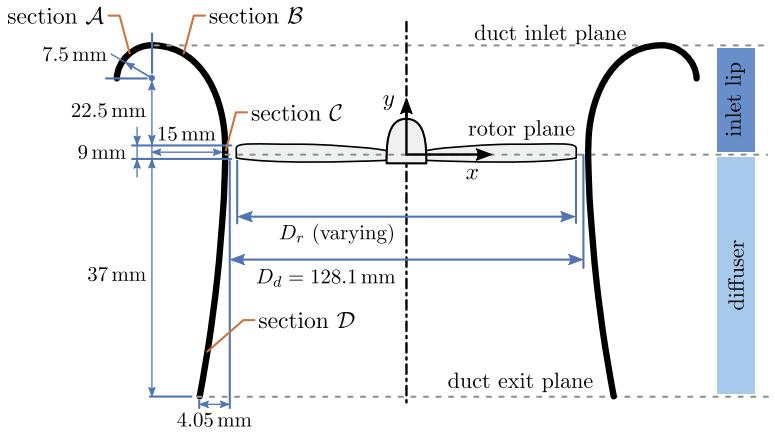

Fig. 14. Schematic of the duct design consisting of four sections. The rotor phase θ is such that $\theta = 0°$ in the displayed position (rotor colinear with the x axis).

jet is relatively faster at the diffuser trailing edge, increasing the high-frequency component.

CRediT authorship contribution statement

Reinier J. Goudswaard: Writing – review & editing, Writing – original draft, Visualization, Validation, Methodology, Investigation, Formal analysis, Conceptualization. **Daniele Ragni:** Writing – review & editing, Validation, Supervision, Methodology, Investigation, Conceptualization. **Woutijn J. Baars:** Writing – review & editing, Visualization, Validation, Supervision, Methodology, Investigation, Conceptualization.

Declaration of competing interest

The authors declare that they have no known competing financial interests or personal relationships that could have appeared to influence the work reported in this paper.

Acknowledgements

We wish to acknowledge Flyability (https://www.flyability.com/) for providing general rotor and duct geometry definitions. We also wish to acknowledge Stefan Bernardy and Emiel Langedijk for technical assistance in realizing the experimental setup in the Flow Physics & Technology laboratory at the Delft University of Technology.

Appendix A. Ducted-rotor system design

The ducted rotor system was provided by Flyability, a company that develops MAV drones for indoor inspection (https://www.flyability.com/). In the pursuit of more efficient propulsion devices, they developed a 5-inch ducted rotor for a quad-copter in hover flight. Both the duct and rotor geometry were optimized to minimize the mechanical power for a certain amount of thrust. For the current study it is a great opportunity to investigate the system provided, as no ducted rotors for hover flight of this scale are commercially available. Fig. 14 provides a cross-sectional view of the design of the axisymmetric duct, including the dimensions of the duct wall. This duct consists of four sections:

1. The outer part of the inlet lip (section $\mathcal{A}$) consists of a quarter circle;
2. from the top part of the duct the wall continues on the inner side of the inlet lip (section $\mathcal{B}$) as a quarter ellipse;
3. a straight line segment (section $\mathcal{C}$) is then centered at the rotor plane, such that the tip gap distance is constant along the complete chord of the rotor tip;
4. the diffuser (section $\mathcal{D}$) consists of a spline tangent to the line above, with an average diffuser angle of 8°.

The duct is 3D-printed with an SLS printer (0.1 mm precision) and sanded/waxed to smoothen the inner surface.

Regarding the 2-bladed rotor, a custom made design was optimized for operation in the duct. Compared to commercially available standard rotors for open air, it has a much more aggressive blade pitch. The adapted pitch distribution ensures that the blade operates at roughly the same angle of attack along its complete span. This is crucial for current study, because the vortex dynamics of the rotor can only be properly investigated if the rotor blade sections operate at the right angle. Furthermore, the chord of the blade (20 mm) remains constant towards the tip, contrary to rotors that are optimized for open air (for rotors in open air the blade chord generally washes out towards the rotor-tip to reduce the losses related to tip vortices). The material of the rotor is injection molded plastic.

Data availability

Data will be made available on request.

References

[1] R.W. Deters, G.K. Ananda, M.S. Selig, Reynolds number effects on the performance of small-scale propellers, in: AIAA Paper 2014-2151, 2014, pp. 1–43.
[2] A. Akturk, C. Camci, Tip clearance investigation of a ducted fan used in VTOL Unmanned Aerial Vehicles—Part I: baseline experiments and computational validation, J. Turbomach. Trans. ASME 136 (2) (2013) 021004, https://doi.org/10.1115/1.4023468.
[3] A. Akturk, C. Camci, Experimental and computational assessment of a ducted-fan rotor flow model, J. Aircr. 49 (2012) 885–897, https://doi.org/10.2514/1.C031562.
[4] P. Martin, C. Tung, Performance and flowfield measurements on a 10-inch ducted rotor VTOL UAV, 20050009943, NASA, 2004, https://ntrs.nasa.gov/citations/20050009943.
[5] J. Pereira, Hover and wind-tunnel testing of shrouded rotors for improved micro air vehicle design, Ph.D. thesis, University of Maryland, Department of Aerospace Engineering, College Park, MD, 2008, https://apps.dtic.mil/sti/tr/pdf/ADA595716.pdf.
[6] H. Bento, R. de Vries, L.L.M. Veldhuis, Aerodynamic performance and interaction effects of circular and square ducted propellers, in: AIAA Paper 2020-1029, 2020, pp. 1–21.
[7] D. Shukla, N. Komerath, Rotor—duct aerodynamic and acoustic interactions at low Reynolds number, Exp. Fluids 60 (2019) 885–897, https://doi.org/10.1007/s00348-018-2668-z.
[8] F. Avallone, D. Ragni, D. Casalino, On the effect of the tip-clearance ratio on the aeroacoustics of a diffuser-augmented wind turbine, Renew. Energy 152 (2020) 1317–1327, https://doi.org/10.1016/j.renene.2020.01.064.
[9] A. Malgoezar, A. Vieira, M. Snellen, D. Simons, L. Veldhuis, Experimental characterization of noise radiation from a ducted propeller of an unmanned aerial vehicle, Int. J. Aeroacoust. 18 (2019) 372–391, https://doi.org/10.1177/1475472X19852952.
[10] P. Santosh, Noise generation mechanisms in short ducted rotors, Master's thesis, The Pennsylvania State University, College of Engineering, State College, PA, Aug. 2011, https://etda.libraries.psu.edu/catalog/11241.
[11] M. Raffael, C. Willert, F. Scarano, C.J. Kähler, S.T. Werely, J. Kompenhans, Particle Image Velocimetry – A Practical Guide, Springer, Berlin, Germany, 2018.

[12] R. Merino-Martínez, et al., Aeroacoustic design and characterization of the 3D-printed, open-jet, anechoic wind tunnel of Delft University of Technology, Appl. Acoust. 170 (2020) 107504, https://doi.org/10.1016/j.apacoust.2020.107504.
[13] C.E. Tinney, J. Sirohi, Multirotor drone noise at static thrust, AIAA J. 56 (7) (2018) 2816–2826, https://doi.org/10.2514/1.J056827.
[14] W.J. Baars, D. Ragni, Low-frequency intensity modulation of high-frequency rotor noise, AIAA J. 62 (9) (2024) 3374–3390, https://doi.org/10.2514/1.J063610.
[15] R.J. Goudswaard, Aerodynamic performance of a small-scale ducted rotor in hover: an experimental study on the effect of the tip gap, Master's thesis, Delft University of Technology, 2021, http://resolver.tudelft.nl/uuid:727fd73b-ddb1-40d9-b7fd-2617f769136d.
[16] C. Keys, M. Sheffler, S. Weinier, R. Herminway, LH wind tunnel testing: key to advanced aerodynamic design, in: American Helicopter Society 47th Annual Forum Proceedings, vol. 152, 1991, pp. 77–87, https://vtol.org/store/product/lh-wind-tunnel-testing-key-to-advanced-aerodynamic-design-860.cfm.
[17] D.B. Hanson, Spectrum of rotor noise caused by atmospheric turbulence, J. Acoust. Soc. Am. 56 (1) (1974) 110–126, https://doi.org/10.1121/1.1903241.